



2nd Advanced Optical Metrology Compendium

Advanced Optical Metrology

Geoscience | Corrosion | Particles | Additive Manufacturing: Metallurgy, Cut Analysis & Porosity



EVIDENT
OLYMPUS

WILEY

The latest eBook from **Advanced Optical Metrology**.
Download for free.

This compendium includes a collection of optical metrology papers, a repository of teaching materials, and instructions on how to publish scientific achievements.

With the aim of improving communication between fundamental research and industrial applications in the field of optical metrology we have collected and organized existing information and made it more accessible and useful for researchers and practitioners.

EVIDENT
OLYMPUS

WILEY

High-Temperature Behavior of the Heat-Treated and Overaged AlSi10Mg Alloy Produced by Laser-Based Powder Bed Fusion and Comparison with Conventional Al–Si–Mg-Casting Alloys

Gianluca Di Egidio,* Alessandro Morri, Lorella Ceschini, and Lavinia Tonelli

In recent years, the AlSi10Mg alloy produced by laser-based powder bed fusion (L-PBF) has gained more attention for increasing the strength-to-weight ratio in structural parts subjected to severe operating conditions. Herein, the effects of thermal exposure (0–48 h at 200, 210, and 245 °C) on the metastable microstructure of the L-PBF AlSi10Mg alloy and the high-temperature (200 °C) tensile properties post-overaging (41 h at 210 °C) of the heat-treated alloy is investigated. In particular, two specific heat treatment conditions, currently neglected in the literature, are analyzed: i) T5 heat treatment (direct artificial aging: 4 h at 160 °C), and ii) the innovative T6R heat treatment (rapid solution: 10 min at 510 °C, and artificial aging: 6 h at 160 °C). The T5 shows a lower decrease in mechanical properties after thermal exposure and during the high-temperature tensile test than the T6R. This behavior is related to the higher efficiency of the submicrometric cellular structure in hindering the dislocation motion. In addition, the T5 has good tensile properties compared to high-temperature Al–Si–Mg- and Al–Si–Cu–Mg-casting alloys, representing an attractive option in future industrial applications characterized by operating temperatures up to 200 °C.

1. Introduction

The continuous research of new technologies and materials to reduce the CO₂ footprint has led to a significant interest in additive manufacturing (AM). In particular, the laser-based powder bed fusion (L-PBF) process represents one of the most attractive technologies currently available for producing complex-shaped components characterized by light structures and high mechanical performance.^[1,2] Transportation and energy are probably the


main industrial sectors that can significantly benefit from reducing the mass and size of mechanical parts manufactured by the L-PBF process to reduce their environmental impact.^[3,4] Fuel injectors, heat sinks, mixing and swirling burner tips, pistons, gas turbines, and aerodynamic parts are, in fact, a few examples of possible L-PBF-produced components.^[5–7] However, thin-walled and lattice design solutions require the continuous development of new thermally stable materials capable of withstanding the thermomechanical stresses caused by the severe operating conditions (high temperatures and long service times) occurring in automotive, aeronautical, aerospace, and energy applications.^[8–10]

Among the metals used in the L-PBF process, the Al–Si–Mg alloys represent an up-and-coming solution for producing structural components.^[11] They meet both mechanical (high strength-to-weight ratio) and production requirements (good fluidity

and weldability) compared to other Al-casting alloys, such as the heat-resistant Al–Cu and Al–Zn alloys.^[12–15] The Si content close to the eutectic point reduces the solidification range and increases the powder bed's laser absorption, thus improving the melt pool (MP) fluidity and simplifying the printing process.^[16] In addition, the high Mg content enables precipitation of the Mg₂Si precursor phases during the printing process, further strengthening the Al matrix.^[17,18]

The AlSi10Mg alloy is currently the most common Al–Si–Mg alloy used in the L-PBF process. The cellular structure of the as-built (AB) L-PBF AlSi10Mg alloy consists of sub-micrometric cells of supersaturated α -Al phase surrounded by a eutectic-Si network, which gives high hardness and tensile strength values at the expense of ductility.^[19–21] However, as widely described by the authors in previous work,^[22] the thermally activated diffusion processes alter the metastable microstructure of the AB alloy, acting on the size and morphology of the dispersed (nano-sized Si precipitates and precursors of the Mg₂Si equilibrium phase) and aggregated (eutectic-Si network) strengthening phases. Consequently, given the complexity of the topic, the literature in recent years has mainly focused on the effects of process parameters and heat treatments on the microstructure and the mechanical properties at room temperature (RT) of the L-PBF

G. Di Egidio, A. Morri, L. Ceschini, L. Tonelli
Department of Industrial Engineering (DIN)
Alma Mater Studiorum
University of Bologna
Viale del Risorgimento 4, 40136 Bologna, Italy
E-mail: gianluca.diegidio2@unibo.it

 The ORCID identification number(s) for the author(s) of this article can be found under <https://doi.org/10.1002/adem.202201238>.

© 2023 The Authors. Advanced Engineering Materials published by Wiley-VCH GmbH. This is an open access article under the terms of the Creative Commons Attribution License, which permits use, distribution and reproduction in any medium, provided the original work is properly cited.

DOI: 10.1002/adem.202201238

AlSi10Mg alloy, omitting the analysis of the effect of long-term exposure at high temperatures (near or higher than 200 °C) on microstructure and mechanical behavior. However, this lack of knowledge concerning the L-PBF AlSi10Mg alloy limits its use in producing directly or indirectly heat-exposed high-tech components.

To the best of the authors' knowledge, only a few studies focused on the high-temperature mechanical behavior of the L-PBF AlSi10Mg alloy in AB or heat-treated conditions. Uzan et al.^[23] evaluated the high-temperature mechanical properties of the L-PBF AlSi10Mg alloy subjected to stress relieving (SR) (2 h at 300 °C) in a range between 25 and 400 °C. In particular, they observed a significant decrease in mechanical strength (yield strength [YS] and ultimate tensile strength [UTS]) and an increase in elongation to failure (e_f) with increasing test temperature. Furthermore, the analysis of the true stress–true strain curves showed strain-hardening phenomena only at temperatures below 200 °C. Lehmus et al.^[24] observed comparable results on the SR alloy (2 h at 350 °C) tested at 125, 250, and 400 °C, reporting a significant reduction in strength above 250 °C and the dominant effect of temperature on building orientation. Tocci et al.^[25] shifted their attention on the L-PBF AlSi10Mg alloy in AB condition and post-thermal exposure (10 h at 100 and 150 °C), observing during high-temperature tensile tests (100 and 150 °C) a slight decrease in UTS, a significant increase in e_f , but no effect on YS. Cao et al.^[26] delved into this topic, evaluating the effect of thermal exposure on the AB alloy up to 400 °C and observing the remarkable increase in e_f due to softening mechanisms at elevated temperatures.

However, as Lehmus et al.^[24] highlighted, further studies should investigate the effects of thermal exposure on the kinetics of microstructural evolution and overaging phenomena, quantifying the high-temperature performances of the L-PBF AlSi10Mg alloy subjected to different heat treatments, that is, direct aging (T5) and solutioning plus artificial aging [AA] (T6).

Therefore, this work aims to fill the knowledge gap on the effects of overaging and high temperatures on the peculiar microstructure

and the tensile properties of the L-PBF AlSi10Mg alloy subjected to an optimized direct aging treatment (hereafter T5) and an innovative rapid solution treatment (hereafter T6R). The heat-treatment conditions were selected based on previous work,^[22] as the T5 slightly increased the mechanical properties of the AB alloy, preserving its microstructure and strengthening mechanisms, while the T6R obtained the best compromise between strength and ductility compared to other conditions assessed.

The results of the high-temperature mechanical characterization were compared to those of previous studies carried out by the authors on various Al-casting alloys developed explicitly for high-temperature applications.^[27–30]

2. Experimental Section

The specimens (bars with a diameter of 9 mm and height of 77 mm) were produced using the SLM500 system (SLM Solution Group AG, DE) on a heated platform (150 °C) under an Ar atmosphere, with a total printing time of approximately 30 h. The samples were removed from the platform by wire electrical discharge machining. The chemical composition and physical properties of feedstock powder and the L-PBF process parameters are reported in Table 1. In particular, the selection of process parameters aimed at achieving the best compromise between building rate and bulk material density to optimize industrial productivity and mechanical properties of the L-PBF-produced components.

L-PBF-produced specimens were subjected to T5 and T6R heat treatment according to the conditions reported in Table 2 and optimized in Ref. [22]. Solution treatment (SHT) and AA were carried out in an electric furnace with a temperature control of ± 5 °C.

Overaging (OA) curves (hardness as a function of temperature and time) evaluated the effects of thermal exposure at 200, 210, and 245 °C (overaging temperatures [T_{OA}]) for an exposure time (t_{OA}) on the T5 and T6R heat-treated alloys, up to a maximum of 48 h. The OA conditions analyzed both the effects on the

Table 1. Chemical composition [wt%] and physical properties of the AlSi10Mg powder supplied by the producer; L-PBF process parameters and scan strategy conditions.

Chemical composition											
Element [wt%]	Al	Si	Mg	Fe	Cu	Mn	Ni	Pb	Sn	Ti	Zn
Powders	Bal.	9.210	0.270	0.150	0.001	0.006	0.003	0.001	<0.001	0.05	0.002
Powder physical properties											
Tap density [g cm^{-3}] American society for testing and materials (ASTM) B527	Carney apparent density [g cm^{-3}] ASTM B417			Relative humidity [%]		Static carney flow test [s (150 g^{-1})] ASTM B964			Powders range size [μm] ASTM B822, B221, B214		
1.80	1.49			4.6%		32			20–63		
L-PBF process parameters											
Atmosphere	Heated platform [°C]	Laser power [W]		Scan speed [mm s^{-1}]	Spot diameter [μm]	Layer thickness [μm]	Hatch distance [μm]	Energy density [J mm^{-3}]			
Ar, $\text{O}_2 < 0,2 \text{ vol}\%$	150	350		1150	80	50	170	36			
L-PBF Scan strategy											
Bidirectional stripes scan strategy of 67° rotation between subsequent layers and remelted contour zone strategy at the end of each scanning											

Table 2. Heat treatment conditions for the L-PBF AlSi10Mg alloy.

Condition	T5	T6R
Heat-treatment sequence	AA at 160 °C for 4 h, air cooling	SHT at 510 °C for 10 min, water quenching at room temperature, AA at 160 °C for 6 h, air cooling

metastable microstructure of the typical average temperatures (200 and 210 °C) experienced by a high-performance motorbike engine during a race^[30] and the effects of peak operating temperature (245 °C) inside the cylinder.^[9]

Hardness values were measured through the Brinell test (hereinafter HB₁₀) with a 2.5 mm diameter steel ball and a 62.5 kgf load, according to the ASTM E10-18 standard.^[31] At least five measurements were performed for each time-temperature combination, then average values and standard deviations were reported in OA curves. A field-emission gun scanning electron microscope (FEG-SEM, TESCAN MIRA3) equipped with energy-dispersive X-ray spectroscopy (EDS) was used for microstructural analysis. Microstructural characterization was performed for each investigated temperature (200, 210, and 245 °C) to observe the microstructural modification induced by thermal exposure. Metallographic samples were embedded in resin, grounded and polished according to ASTM E3,^[32] and chemically etched with Weck's reagent (3 g NH₄HF₂, 4 mL HCl, 100 mL H₂O) according to ASTM E407.^[33] Image analysis, aimed at determining quantitative parameters of the Si particles present in the T6R alloy, was carried out by the ImageJ software on 5 images at 7.5kx magnification for a total area of about 4 × 10⁻³ mm², according to Ref. [34].

High-temperature (200 ± 5 °C) tensile tests were carried out on T5 and T6R alloys after OA at 210 °C for 41 h (T5_{OA} and T6R_{OA}). OA conditions for tensile tests were chosen to reproduce the average operating conditions typical of racing engine heads.^[30] Four-round dog-bone specimens for each tested condition were considered and machined from L-PBF-produced bars (Figure 1). A screw testing machine, equipped with a resistance furnace and a high-temperature strain gauge, performed the tests at a strain rate of 3.3 × 10⁻³ s⁻¹ according to ISO 6892-1 and ISO 6892-2.^[35,36] The heating rate in the furnace reached the testing temperature (200 ± 5 °C) within 30 min. Once reached the testing temperature, the specimens were maintained at 200 °C for 30 min before starting the tensile test to homogenize the temperature in the whole specimen. Two K-type thermocouples were placed next to the specimen in the upper and bottom zones of the calibrated gauge length to check the temperature's

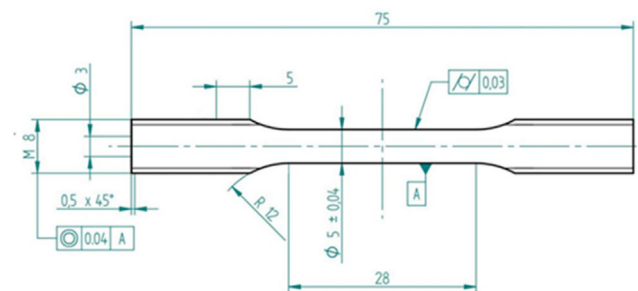


Figure 1. Tensile sample geometry (dimensions in millimeter).

uniformity during the furnace's holding time. The temperature was maintained at 200 °C until the failure of the sample. After the high-temperature tensile tests, the residual hardness of the sample was evaluated by five HB₁₀ measurements.

Results of high-temperature tensile tests were compared to RT tensile properties reported in Ref. [22] and to previous mechanical characterizations carried out by the authors on other Al-casting alloys.^[29,30] The plastic behavior of the L-PBF AlSi10Mg alloy was described by Hollomon's equation (Equation (1)) to study the effects of OA and high-temperature test on the strain-hardening ability of L-PBF AlSi10Mg alloy^[4,37]

$$\sigma = K\epsilon^n \quad (1)$$

The elastic strain was subtracted from the total strain for calculation of the true strain according to ISO 10 275 standard.^[38] The strength coefficient *K* and the hardening exponent *n* were evaluated using true stress–true strain data between 2% plastic strain and the percentage plastic extension at maximum force.^[38]

Fractographic analyses, carried out using the FEG–SEM, highlighted the differences in fracture mechanisms among samples tested at RT and high temperature.

3. Results and Discussion

3.1. Effects of Overaging on Hardness and Microstructure

OA curves (Figure 2) describe the effects of high-temperature exposure on the L-PBF AlSi10Mg alloy. Hardness measurements were performed on T5 (Figure 2a) and T6R (Figure 2b) samples exposed at 200, 210, and 245 °C up to a maximum of 48 h.

At 200 and 210 °C, the T5 alloy shows a comparable slight decrease (about 1 HB₁₀ h⁻¹) in the first 8 h from the initial hardness (122 HB₁₀). However, for longer exposure times (up to 48 h), the drop is more significant at 200 °C (106 HB₁₀ (–13%)) than at 210 °C (98 HB₁₀ (–20%)). Instead, at 245 °C, the T5 alloy reaches 91 HB₁₀ in just 8 h (–25%), while in the following 40 h arrives at the minimum value of 80 HB₁₀ (–35%) (Figure 2a). These different performances can be explained in light of the microstructural evolution induced by OA.^[39,40] Therefore, AB and T5 microstructures before and after exposure to 200, 210, and 245 °C for 48 h (hereafter T5–200 °C, T5–210 °C, and T5–245 °C, respectively) are shown in Figure 3.

AB and T5 alloys have very similar microstructures,^[22] constituted by an ultrafine sub-micrometric structure of supersaturated α-Al cells surrounded by a eutectic-Si network (Figure 3a,b) resulting from the high solidification rate.^[41,42] Furthermore, Si forms nano-sized precipitates inside the α-Al cells^[39,43] and Mg₂Si precursors phases (β' and β'') by reacting with Mg, which mainly segregates in the intercellular network along cell boundaries.^[41,43] Unfortunately, the high-strength

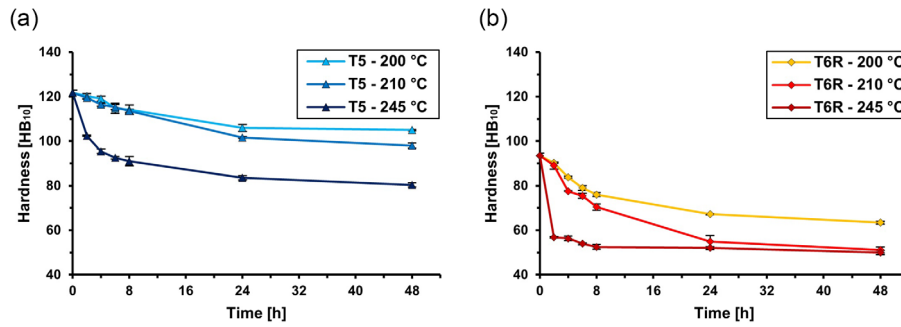


Figure 2. Overaging (OA) curves at 200, 210, and 245 °C for a) T5 and b) T6R.

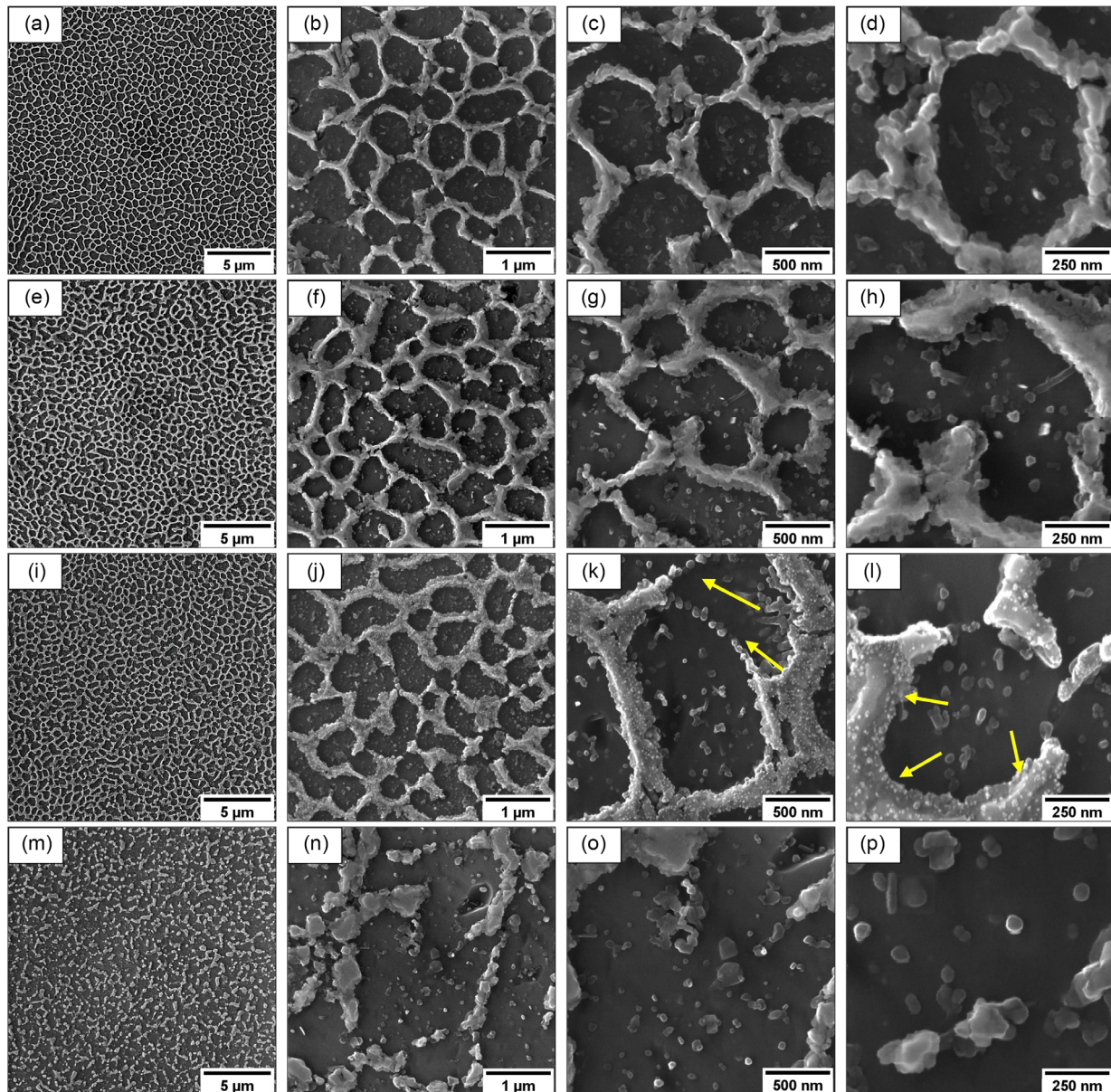


Figure 3. T5 microstructures: a–d) before OA, e–h) T5–200 °C, i–l) T5–210 °C, m–p) T5–245 °C. Yellow arrows in k) and l) highlight the Si nanoparticles anchored to the eutectic-Si network due to the activation of diffusion processes, which promote the formation of spherical Si-rich particles in the α -Al matrix at 245 °C.

microstructure is metastable and evolves toward a more stable but less performing condition during prolonged exposure to high temperatures.^[21,40,44]

At low magnification (Figure 3a,e,i,m), microstructural modifications become appreciable only for the T5–245 °C. In this case, the dissolution of the Si network leads to the fragmentation into numerous irregular Si-rich particles and a decrease in the strengthening effect by microstructural refinement and fine-aggregated second phases (Figure 3n). The evolution in the microstructure, which is schematized in **Figure 4**, is close to the one observed in the L-PBF AlSi10Mg alloy subjected to SR heat treatment, which is generally performed at 300 °C for 1–2 h.^[19,20,45] Furthermore, the diffusion processes of Si atoms, activated by the highest T_{OA} , lead to the coarsening of the nano-sized Si particles in the α -Al matrix (Figure 3o,p).

Evident changes in the eutectic-Si network as a consequence of thermal exposure can be observed at higher magnifications starting from the T5–210 °C. Figure 3k,l shows the initial dissolution step of the eutectic-Si network, which appears partially fragmented and shows Si nanoparticles anchored to its branches. During the diffusion processes, the Si atoms move from the eutectic-Si network to the Al matrix to form new Si particles and coarse preexisting nano-sized Si particles to minimize the internal energy of the microstructure.^[21,44] As a result, the Si network begins to shrink while the Si particles continue to coalesce and develop.^[46] The T5–200 °C does not show this phenomenon (Figure 3g,h), and the eutectic-Si network has a homogeneous and smooth structure (Figure 3c,d). Even though the T5–200 °C and T5–210 °C have a eutectic-Si network characterized by different morphology (Figure 3b,f,j,n), the micrographs show a similar density of Si particles within the α -Al cells, confirming that the diffusion of Si atoms from the eutectic-Si network to the Al matrix takes place also at 200 °C.^[39,40,47] Instead, the higher diffusion rate in the T5–245 °C promotes the formation of larger nano-sized Si particles compared to the T5–200 °C and T5–210 °C.

Even though TEM analysis would be necessary for evaluating the effects of OA on nano-sized Si- and Mg₂Si-strengthening precipitates, several authors agree that prolonged thermal exposure generates diffusion-driven phenomena and a rapid coarsening of the reinforcing precipitates (Ostwald ripening mechanism) in heat-treated Al-casting alloys^[8,9,27,28,30] and heat-treated L-PBF AlSi10Mg alloy.^[17,20,47] These phenomena lead to a microstructure containing larger but fewer precipitates that offer less

contribution to alloy strengthening and hardness due to 1) lower precipitate/matrix interfacial area; 2) lower density of obstacle to dislocation motion, and 3) lower coherence between the strengthening precipitates and α -Al matrix.

OA curves of the T6R alloy (Figure 2b) show a significant decrease in hardness after 48 h for all the investigated temperatures: 1) –19% at 200 °C, 2) –25% at 210 °C, and 3) –44% at 245 °C. At 245 °C, the drop in hardness occurs almost immediately: after 2 h, the residual hardness equals 57 HB₁₀, close to the minimum value of 51 HB₁₀ measured after 48 h. OA curves at 200 and 210 °C show different trends: they start from a comparable decrease in hardness (2.2–2.9 HB₁₀ h^{–1}) up to 8 h, however, differing for longer soaking times. In particular, at 200 °C, the T6R alloy reaches a minimum value of 63 HB₁₀ in the following 40 h. Conversely, at 210 °C, it shows a value of 55 HB₁₀ after only 24 h, very close to the residual hardness after 48 h (51 HB₁₀).

The T6R microstructures before and after thermal exposure at 200, 210, and 245 °C for 48 h (hereafter T6R–200 °C, T6R–210 °C, and T6R–245 °C, respectively) are reported in **Figure 5**.

The microstructure of the T6R alloy consists of a composite-like microstructure of Si-rich particles embedded into the α -Al matrix (Figure 5a).^[22] During the SHT step, two different solid-state diffusion-driven mechanisms lead to the fragmentation of the eutectic-Si network, the spheroidization of Si, and the coarsening of the nano-Si precipitates, that is, 1) the surface self-diffusion, in which the atoms move by surface diffusion, and 2) the interdiffusion at the Al/Si interface, in which the Si atoms move through the Al matrix.^[44] In addition, during the AA step, the precipitation of both β'' - and β' -strengthening phases (precursors of the Mg₂Si equilibrium phase) occurs, introducing precipitation hardening.^[17,42] Therefore, OA could have two main effects on the microstructure: 1) modification of the size of the Si particles developed during the SHT^[16,21,46] and 2) coarsening of the Mg₂Si coherent precipitates obtained during the AA^[13,44,48].

In the T6R–200 °C, a minimal change in Si particle size and distribution (**Figure 6a,b**) is visible, as confirmed by Si interparticle spacing (**Table 3**). Despite the low increase in T_{OA} , the T6R–210 °C (Figure 5c) shows a remarkable increase (+14%) in Si particle size (Figure 6a), a decrease in the number of Si particles per unit area (–18%) (Figure 6b) and an increase in Si particle interspacing (+9%) (Table 3) compared to the T6R. As expected, the T6R–245 °C shows the most significant

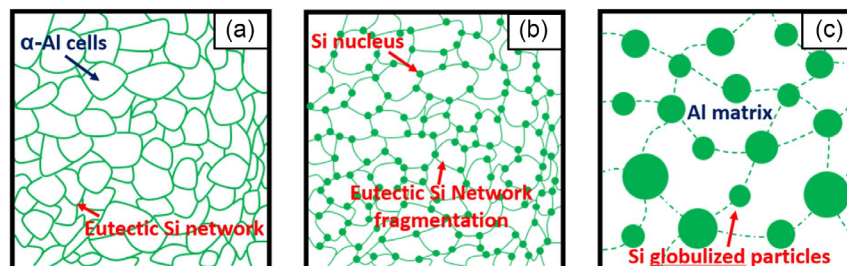


Figure 4. Scheme of the microstructural evolution in the T5 alloy induced by thermal exposure: a) before OA, the continuous eutectic-Si network surrounds the sub-micrometric cells of supersaturated α -Al phase; b) during the first phases of thermal degradation, fragmentation of the eutectic-Si network and the consequent formation of the first Si nucleus occur; c) as the thermal exposure continues, coarsening of the first Si nucleus brings to the formation of the Si particles embedded into the α -Al matrix (if T_{OA} and t_{OA} are sufficient).

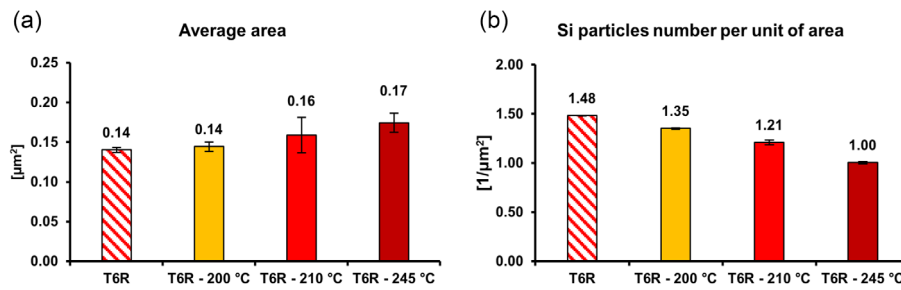


Figure 6. a) Effects of OA (200, 210, and 245 °C for 48 h) on Si particle average area and b) the number of Si particles per unit of area of the T6R alloy.

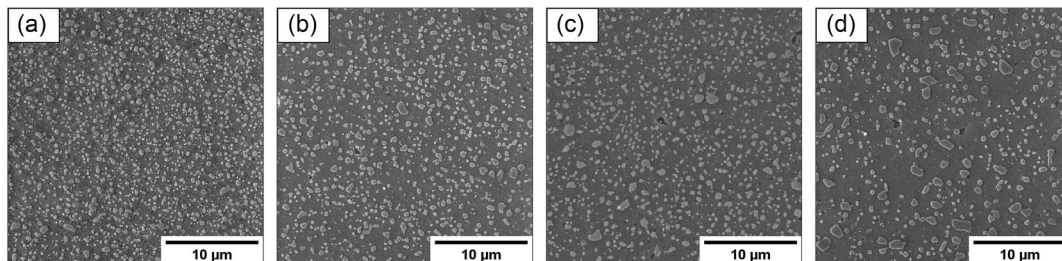


Figure 5. Si particle characterization of the T6R alloy evaluated: a) before OA, b) after OA at 200 °C, c) 210 °C, d) and 245 °C for 48 h.

Table 3. Interparticle spacing (λ) and interparticle spacing variation ($\Delta\lambda$) compared to the T6R alloy for the different OA conditions.

Condition	λ [μm]	$\Delta\lambda$ [μm]	Percentage increase
T6R	0.57 ± 0.02	–	–
T6R–200 °C	0.58 ± 0.01	0.01	1.8%
T6R–210 °C	0.62 ± 0.03	0.05	8.8%
T6R–245 °C	0.65 ± 0.04	0.08	14.0%

effects on the T6R microstructure. The higher T_{OA} leads to a further increase in Si particle size (+21%) (Figure 6a), a decrease in the number of Si particles per unit area (–32%) (Figure 6b), and an increase in Si particle interspacing (+14%) (Table 3) compared to the T6R.

Even though microstructural analyses can easily observe the coalescence of the Si particles, its effect on the hardness of the T6R alloy is negligible compared to the coarsening of the strengthening precipitates. In previous authors' work,^[22] an increase of the Si particle size up to 300% led to a hardness decrease of only 3% in the T6 peak-aged condition. Therefore, the decrease in hardness is probably due to the coarsening of the Mg_2Si -strengthening precipitates. Furthermore, OA curves suggest that thermal exposure at 210 °C for 24 h or at 245 °C for 8 h promotes the formation of incoherent $\beta\text{-Mg}_2\text{Si}$ phase, while at 200 °C only a partial coarsening of the strengthening precipitates occurs.

In summary, for the same T_{OA} and t_{OA} conditions, T5 shows a lower hardness decrease than T6R. Therefore, the sub-micrometric cellular structure of T5 appears to be more capable of hindering the dislocation motion than the composite-like microstructure of T6R, even after long thermal exposure.

3.2. Tensile Tests

Tensile tests were performed at 200 °C on overaged (210 °C for 41 h) samples to compare the results of the tests with the experimental data of previous mechanical characterizations carried out by the authors on Al-casting alloys.^[27–30,49]

3.2.1. Tensile Properties

The results of tensile tests at RT (T5–RT and T6R - RT) and high temperature (T5_{OA}–200T and T6R_{OA}–200T) performed on the L-PBF AlSi10Mg alloy are reported in Figure 7. Hardness measurements were carried out on all specimens after tests. Representative engineering stress–strain curves and corresponding true stress–true strain curves are reported in Figure 8 and compared to AB curves from Ref. [22].

At RT, the T5–RT presents stress–strain curves almost superimposed on AB–RT; as described in Ref. [22], the T5 heat treatment slightly increases the tensile properties of the AB alloy by precipitation hardening, preserving its plastic behavior. In contrast, the T6R heat treatment significantly increases the strength–ductility balance by completely changing the plastic deformation mechanisms of the material.

As expected, the specimens overaged and tested at 200 °C show an evident decrease in YS, UTS, and hardness values compared to the RT specimens, respectively, –42%, –60%, and –18% for the T5_{OA}–200T, and –65%, –70%, and –42% for the T6R_{OA}–200T. Conversely, the ϵ_f showed a significant increase (+65%) for the T5_{OA}–200T but a negligible increase for the T6R_{OA}–200T.

According to microstructural analyses (Figure 3), the decrease in tensile properties (YS and UTS) for the T5_{OA}–200T condition is mainly due to 1) partial or total fragmentation of the eutectic-Si

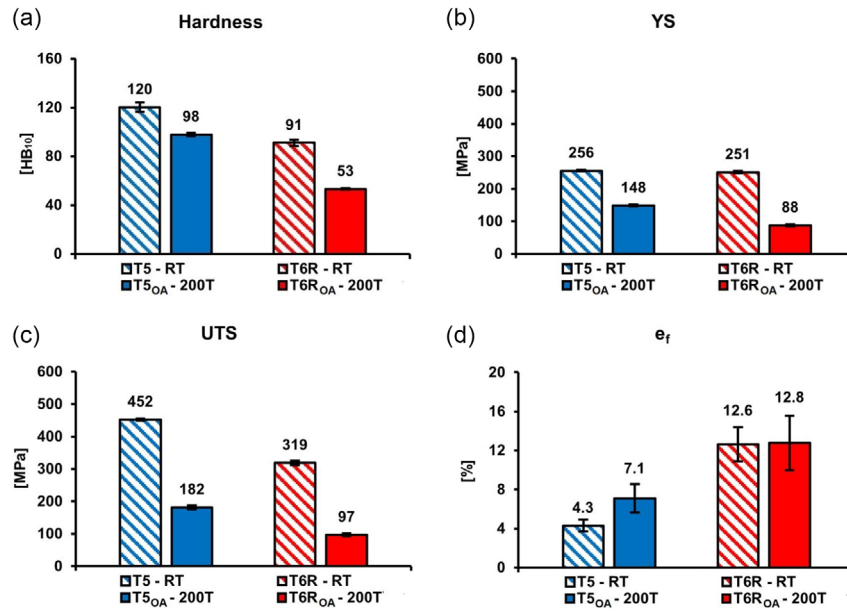


Figure 7. a) Hardness and b–d) tensile properties (yield strength [YS] (b), ultimate tensile strength [UTS] (c), and e_f (d)) of the T5 and T6R alloy tested at i) room temperature (RT) (T5–RT and T6R–RT) and ii) high temperature (T5_{OA}–200T and T6R_{OA}–200T).

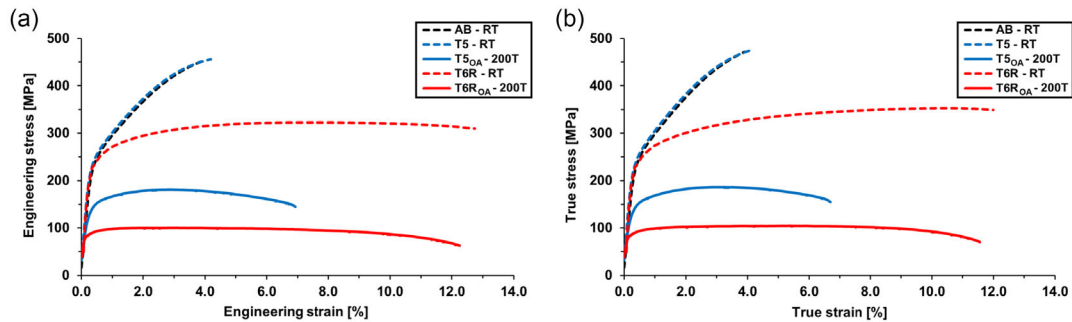


Figure 8. a) Representative engineering stress–strain curves and b) true stress–true strain curves of the T5 and T6R alloy tested at i) RT (T5–RT and T6R–RT) (dashed lines) and ii) high temperature (T5_{OA}–200T and T6R_{OA}–200T) (solid lines). Data is compared to the as-built (AB) curves tested at RT. The elastic strain is subtracted from the total strain for calculation of the true strain according to ISO 10 275:2020 standard.^[40]

network, 2) coarsening of the nano-sized Si precipitates and precursors of the Mg₂Si equilibrium phase, and 3) reduction of Si atoms in solid solution. These changes in the strengthening mechanisms lead to decreased strength and increased ductility due to the lower pinning effects on the dislocation motion. Moreover, during the high-temperature tensile test, softening of the Al matrix occurs, decreasing the activation energy for the dislocation motion and increasing the number of activated sliding planes. This phenomenon stimulates the dislocation motion by climbing and gliding compared to pileup phenomena, leading to increased ductility.^[49–51]

For the T6R_{OA}–200T, the loss of precipitation hardening is the leading cause of the decrease in YS, UTS, and hardness values. Conversely, the negligible effect of OA and high-temperature testing conditions on the e_f is probably attributable to an inhomogeneous and localized plastic deformation of the α -Al matrix that, from a macroscopic point of view, avoids an increase in uniform deformation, as observed in the T5_{OA}–200T. This aspect

will be further described in the following sections concerning the plastic behavior of the material and the fracture surface analyses.

3.2.2. Plastic Behavior

T5 and T6R alloys show a different mechanical behavior evidenced both by the work-hardening exponent (Figure 9), which was evaluated by the true stress–true strain curves in Figure 8b, and by the analysis of the elastic, plastic, and necking fields reported in Figure 10, which was evaluated by the engineering stress–strain curves (Figure 8a).

As is well known, engineering stress–strain curves can be divided into three fields: elastic (up to YS), plastic (uniform strain) from YS to UTS, and necking (localized strain) from UTS to failure (Figure 10a). The stress–strain ratio increases linearly in the elastic range until the dislocation slip. As dislocation

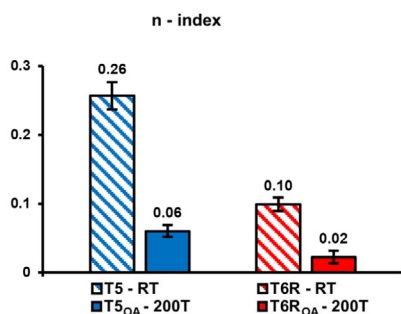


Figure 9. Work-hardening exponent evaluated for the T5 and T6R alloy tested at i) RT (T5–RT and T6R–RT) and ii) high temperature (T5_{OA}–200T and T6R_{OA}–200T).

interactions increase, uniform plastic deformation and work-hardening until necking occur.^[37] The different extension of these three regions of the tested samples is shown in Figure 10b as the ratio between the extension of the single strain field and the total strain field.

In the T5–RT, necking is substantially absent (Figure 8b and 10b). In particular, the high percentage of uniform elongation compared to the total elongation (85%) is evidence of the high strain-hardening ability (Figure 9). As described by Considère’s criterion,^[42] strain-hardening delays the localized deformation and, therefore, the necking phenomenon. In the T5–RT, failure occurs during strain-hardening and before necking due to the high dislocation density and the presence of defects such as porosities or lack of fusions.^[42,52,53] Conversely, the T6R–RT shows a low strain-hardening value (Figure 9) and a significant tendency to necking (Figure 8b and 10b). The T6R microstructure is, in fact, less effective in hindering the dislocation motion than the microstructure of the T5 one. This difference limits the formation of a high density of dislocations in small areas, inducing lower n-index values.^[42]

The T5_{OA}–200T and T6R_{OA}–200T are characterized by i) lower n-index values than T5–RT and T6R–RT, respectively, equal to –77% and –80% (Figure 9); ii) higher necking, respectively, equal to +55% and +76% of the total strain field (Figure 10b). The combined effects of OA and high testing temperature modify

the plastic deformation mechanisms. They increase the localized deformation phenomenon because of 1) the thermal softening of the α -Al matrix occurring at high temperatures, 2) the increase of vacancies by diffusion phenomena, and 3) the loss in efficiency of the strengthening mechanisms.^[37,54,55]

However, the T5_{OA}–200T preserves a minimal strain-hardening ability, thanks to the ultrafine cellular structure still present at high temperatures (Figure 3i).^[43] In contrast, the T6R_{OA}–200T loses almost wholly the strain-hardening ability due to the decrease in the strengthening effect of the Mg₂Si precipitates induced by the high temperature.^[24,28,37]

3.3. Fractography

In this section, the effects of OA and high temperatures are evaluated by comparing the fracture surfaces of the samples tested at 200 °C (T5_{OA}–200T and T6R_{OA}–200T) and the samples tested at RT (T5–RT and T6R–RT).

At low magnification, the fracture surfaces of the T5–RT and T5_{OA}–200T show comparable fracture morphology (Figure 11a,b, e,f), consisting of 1) interlayer fracture path at the eutectic-Si network/Al matrix interface, 2) presence of defects, in particular gas pores, and 3) flat fracture morphology in correspondence of the scan-track segments.^[19] However, the effects promoted by OA and high testing temperature, including the Al matrix softening and the lower cohesion between Al cells and the eutectic-Si network, determine more significant plastic deformation and the formation of larger dimples.^[30,37,48]

At higher magnification (Figure 11c,d,g,h), the T5–RT and T5_{OA}–200T show shallow micro- and sub-micrometric dimples, reflecting the sub-cellular microstructure. Where the eutectic-Si network is continuous and not fragmented, the microstructure is more effective in hindering dislocation slip and reducing the plastic deformation area^[55] and develops small dimples proportional in size to the spacing of the aggregated second phase.^[56] A partially fragmented and coarsened cellular structure leads, instead, to the formation of larger dimples, as observed in the T5_{OA}–200T. To explain this fracture behavior, it is worth noting that the void initiation at the Si network/ α -Al cell interface is an energetic process where a threshold value of work “W” is necessary to create the crack between the aggregated second phase and

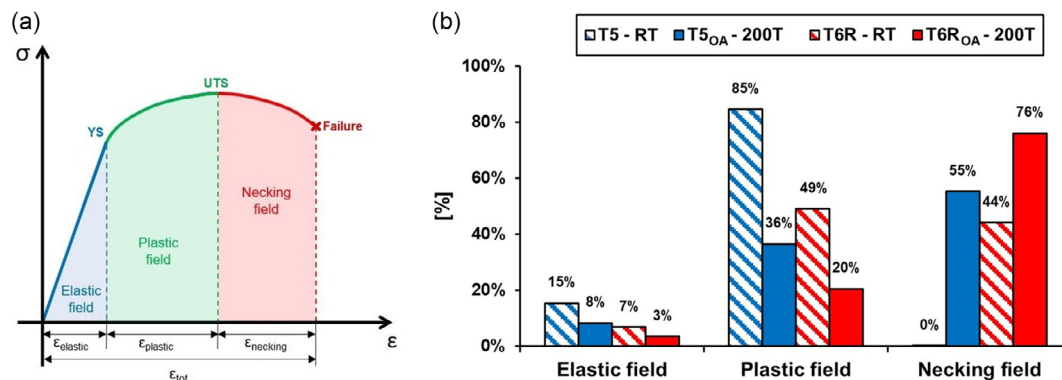


Figure 10. a) Schematic subdivision in the engineering stress–strain curves of the total strain (ϵ_{tot}) into elastic ($\epsilon_{elastic}$), plastic ($\epsilon_{plastic}$), and necking ($\epsilon_{necking}$) fields. b) Percentage subdivision of the stress–strain curves into elastic, plastic, and necking fields for the T5 and T6R alloy tested at RT (T5–RT and T6R–RT), and high temperature (T5_{OA}–200T and T6R_{OA}–200T).

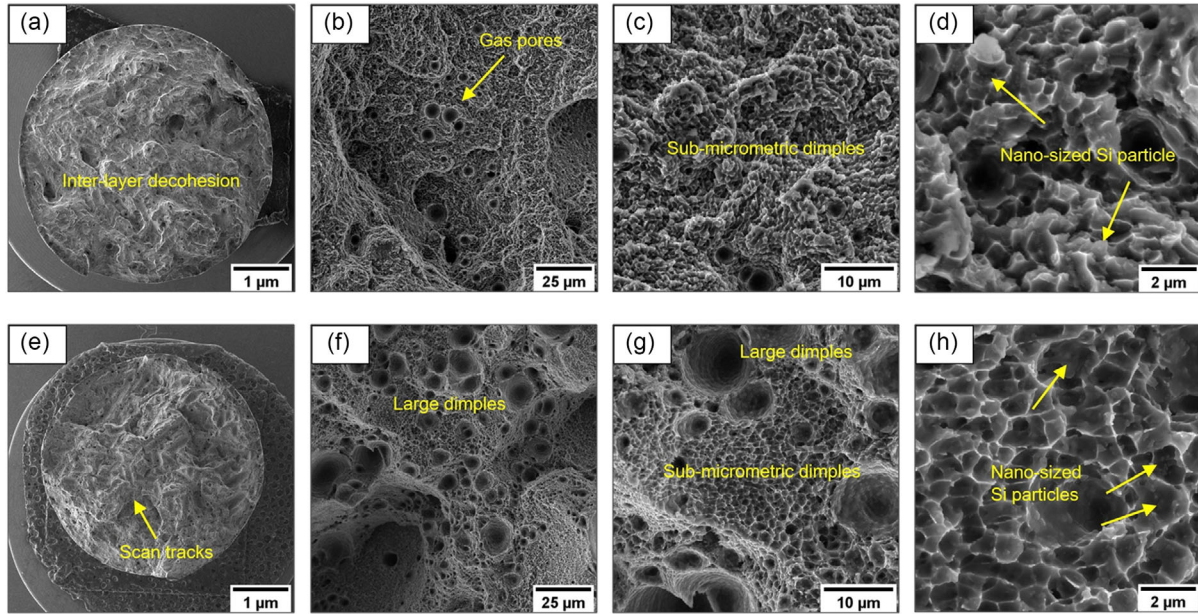


Figure 11. Field-emission gun scanning electron microscope (FEG-SEM) images of the fracture surfaces of the T5-RT and T5_{OA}-200T samples at different magnifications: a,e) 40x, b,f) 1.50kx, c,g) 5.00kx, d,h) and 20.0kx, respectively.

the Al matrix. W depends on three factors: the surface energy of the matrix γ_{Al} , the surface energy of the aggregate second phase γ_{Si} , and the interface energy γ_{Al-Si} (Equation (2)).^[52]

$$W \propto \gamma_{Al} + \gamma_{Si} + \gamma_{Al-Si} \quad (2)$$

Dissolution of the eutectic-Si network at high temperatures increases the strain field due to the difference in the lattice parameters of the Si and Al and the lower coherency between the harder-Si phase and the softer-Al matrix.^[50,52] Those two phenomena increase γ_{Al-Si} , thus reducing the work necessary to nucleate a void at the α -Al matrix/second-phase interface.

The effectiveness of this microstructure at high temperatures explains the lower percentage decrease in strength properties of the T5_{OA}-200T compared to the T6R_{OA}-200T. At the same time, the local increase in plastic flow at the α -Al cell/eutectic-Si network interface, and in particular around the fragmented zones where larger dimples are present (Figure 11e,f), is likely the cause of necking and increase in the ϵ_f value for the T5_{OA}-200T compared to the T5-RT.

The T6R-RT and T6R_{OA}-200T (Figure 12a,b,e,f) exhibit at low magnification a higher gas pore density on the fracture surfaces, compared to the T5_{OA}-200T and T5-RT, probably due to the effects of the SHT.^[57] The T6R-RT shows scan tracks on the fracture surfaces, which are not detected on the T6R_{OA}-200T due to the irregular morphology induced by the necking.

For the T6R-RT and the T6R_{OA}-200T, the fracture propagates by joining gas pores and the voids present at the Si particles/ α -Al matrix interface with a similar mechanism described for the T5_{OA}-200T and reported in Ref. [22]. The morphology, size, number, and distribution of the Si particles strongly influence the decohesion phenomena within the α -Al matrix and the size and depth of the dimples (Figure 12c,d,g,h).^[58,59] The coarsening

of Si particles and the material softening lead to larger dimples in the T6R_{OA}-200T than in the T6R-RT. The effect of the large Si particles on the local plastic deformation of the alloy can be observed in Figure 12g,h; these clearly show the plastic flow of the Al matrix around the Si particles, which are located at the center of the dimples. The formation of larger dimples in the T6R_{OA}-200T may explain the negligible increase in ϵ_f compared to the T6R-RT, despite the matrix softening.^[59] The deformation in the T6R_{OA}-200T is not homogeneous, and it concentrates around the largest Si particles due to the higher local plastic flow (Figure 12e),^[37,50] thus reducing the uniform strain of the material, as highlighted by the data reported in Figure 10b.

3.4. Comparison between the High-Temperature Performance of the L-PBF AlSi10Mg Alloy and Al-Si-Casting Alloys

In this section, the tensile behavior at RT and 200 °C on overaged samples (210 °C for 41 h) (200T) of the T5 and T6R alloy is compared to the A356 (Al-Si-Mg ternary alloy), A354, C355, and A357 + Cu (Al-Si-Mg-Cu quaternary alloys)-casting alloy, whose composition are reported in Table 4. The casting alloys considered in this comparison were subjected to the hot isostatic pressure (HIP) process, which is commonly used in the production of high-value-added-casting components to reduce the internal volume of solidification defects (e.g., gas pores or interdendritic shrinkages), and to the T6 heat treatment.^[27-30]

Different chemical compositions directly affect the mechanical behavior of the casting alloys. The T6 hot isostatic pressed (T6-HIPped) Al-Si-Mg alloys have excellent strength-ductility balance and technological properties,^[8] but they exhibit a lower high-temperature mechanical strength than T6-HIPped Al-Si-Mg-Cu alloys.^[27] The Mg₂Si precipitates (β'' and β' phases), in fact, quickly undergo a diffusion-controlled

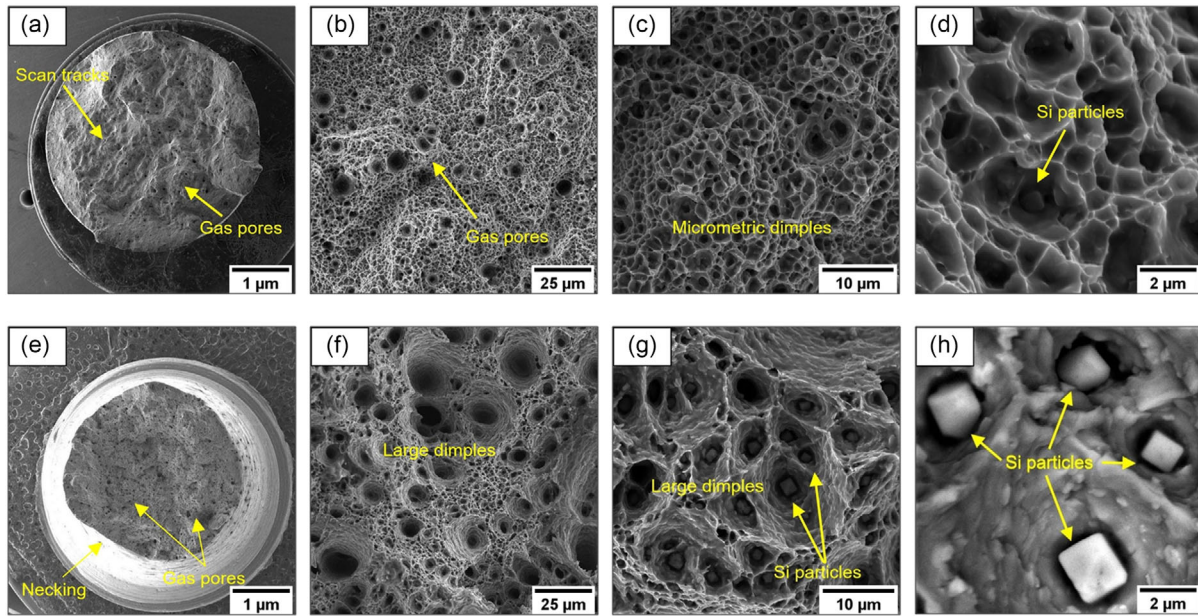


Figure 12. FEG-SEM images of the fracture surfaces of the T6R–RT and T6R_{OA}–200T samples at different magnifications: a,e) 40x, b,f) 1.50kx, c,g) 5.00kx, d,h) and 20.0kx, respectively.

Table 4. Average chemical compositions [wt%] of A354-, A356-, A357 + Cu-, and C355-casting alloys reported in Ref. [27,30] and L-PBF AlSi10Mg alloy used in this study.

Chemical composition												
Element [wt%]	Al	Si	Mg	Fe	Cu	Mn	Pb	Sn	Sr	Ti	B	Zn
A354	Bal.	8.470	0.444	0.135	1.57	0.001	–	–	0.0240	0.126	<0.0002	–
A356	Bal.	7.240	0.420	0.138	<0.001	0.007	–	–	150 ppm	0.120	–	–
A357 + Cu	Bal.	6.770	0.658	<0.03	1.290	<0.001	–	–	140 ppm	0.05	–	–
C355	Bal.	4.990	0.470	0.138	1.050	0.021	–	–	210 ppm	0.133	0.001	–
L-PBF AlSi10Mg	Bal.	9.662	0.285	0.120	–	0.006	0.008	0.025	–	0.017	–	0.042

coarsening, which leads to a progressive loss of effectiveness in hindering the dislocation slip and lower mechanical strength in OA conditions.^[30] Conversely, in the T6-HIPped Al–Si–Mg–Cu alloys, the presence of Cu and Mg leads to the formation of the β'' and β' phases, but above all of binary CuAl_2 (θ'' and θ'), ternary Al_2CuMg (S'' and S' phases), and quaternary $\text{Al}_5\text{Mg}_8\text{Cu}_2\text{Si}_6$ (Q'' and Q') precipitates, which are characterized by higher resistance to thermal coarsening than the Mg_2Si ones.^[60,61]

The residual hardness after 48 h at 200 and 245 °C and the mechanical properties at RT and high-temperature post-OA (200T) highlight that the T5 alloy is characterized by 1) a residual hardness higher than the Al–Si–Mg and comparable to the Al–Si–Mg–Cu alloys (Figure 13a,b); 2) lower YS than Al–Si–Mg–Cu and higher than Al–Si–Mg alloys in both conditions (RT and 200T) (Figure 14a); 3) higher UTS than Al–Si–Mg–Cu and Al–Si–Mg alloys value in RT condition, lower UTS than Al–Si–Mg–Cu and higher than Al–Si–Mg alloys in 200T condition (Figure 14b); 4) lower e_f than Al–Si–Mg–Cu and Al–Si–Mg alloys in both conditions (RT and 200T), except for

A354 + Cu-casting alloy (Figure 14c). The additional strengthening mechanisms (aggregated second phases and solid solution) in the T5 alloy are more effective than the T6-HIPped A356 alloy in maintaining a high YS value even at high temperatures but less effective than T6-HIPped Al–Si–Cu–Mg alloys. At the same time, the different UTS and e_f values of the T5–RT condition compared to the casting alloys considered in this study may be attributable to its peculiar ultrafine microstructure.^[22,42]

The T6R alloy is characterized by 1) the lowest residual hardness post-OA (Figure 13a,b), which is comparable only to the T6-HIPped A356 alloy; 2) lower YS and UTS values and higher e_f than Al–Si–Mg–Cu alloys in both tested conditions (RT and 200T) (Figure 14a–c); 3) higher tensile properties (YS and UTS) than the T6-HIPped A356 alloy and comparable e_f in RT condition, but lower mechanical properties (YS, UTS, and e_f) than the T6-HIPped A356 alloy in 200T condition (Figure 14a, b,c). The microstructures of the T6R alloy (composite-like microstructure of Si-rich particles embedded into the α -Al matrix) and the Al–Si–Mg-casting alloys (α -Al dendrites surrounded by

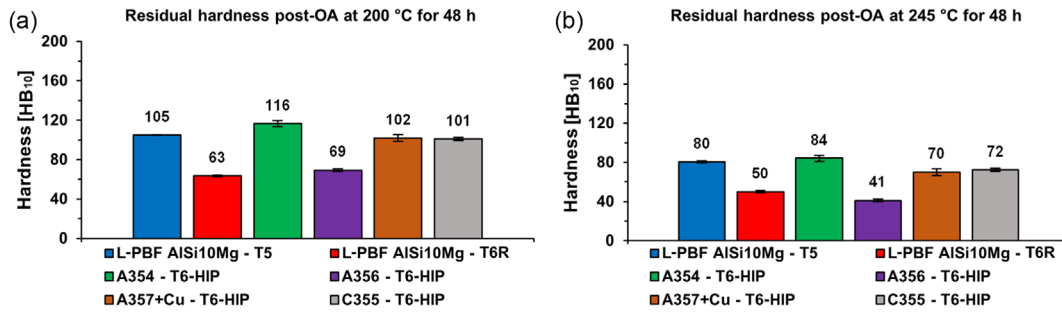


Figure 13. Comparison of the hardness values measured on the T5 and T6R alloy and the T6 hot isostatic pressed (T6-HIPped) Al–Si-casting alloys.^[27,30] The analyzed conditions are post-OA at a) 200 °C and b) 245 °C for 48 h.

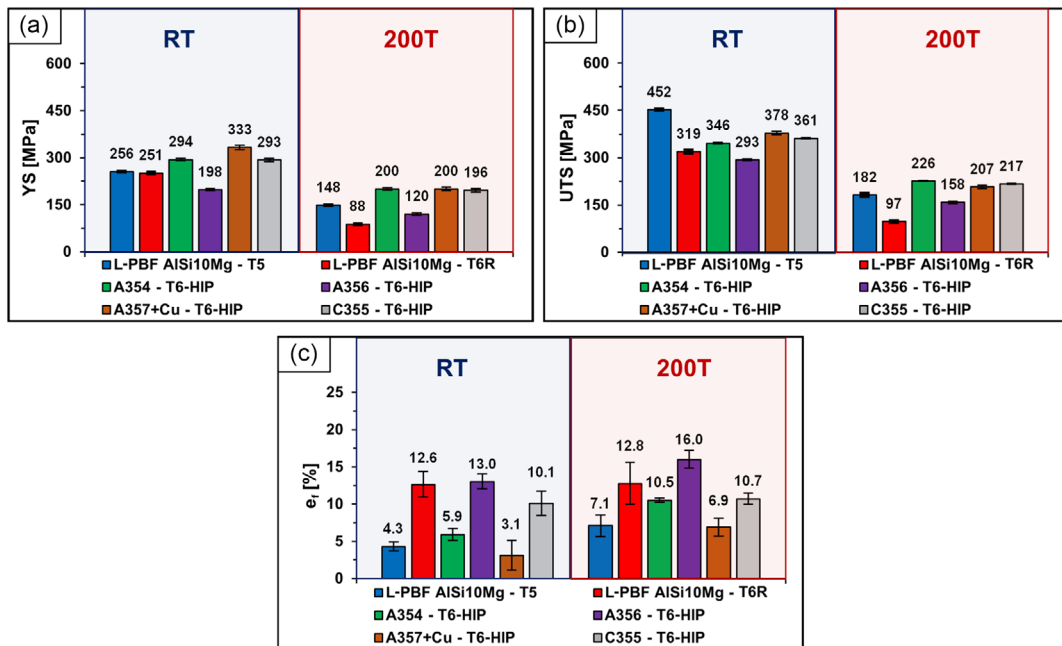


Figure 14. a–c) Room-temperature (RT) and high-temperature (200 °C) tensile properties (a) YS, b) UTS, c) and ϵ_f in overaged conditions (210 °C for 41 h) (200T) of the T5 and T6R alloy and the T6-HIPped Al–Si-casting alloys.^[27,30]

eutectic Al–Si) differently hinder the dislocation motion at high temperatures, and a direct comparison will be certainly necessary to understand the mechanisms involved.

4. Conclusions

The research activity of the present paper aimed to identify the effects of overaging on the microstructure and the mechanical properties of the L-PBF AlSi10Mg alloy subjected to two different heat treatments: T5 (AA at 160 °C for 4 h) and T6R (rapid solution at 510 °C for 10 min followed by AA at 160 °C for 6 h). The effects of the thermal exposure were evaluated at different temperatures (200, 210, and 245 °C) up to a maximum of 48 h. The tensile properties were evaluated at 200 °C on T5 and T6R samples after 41 h at 210 °C (T5_{OA}-200T and T6R_{OA}-200T). Furthermore, fractographic analysis was carried out to identify

the effect of OA and high temperature on the alloy's plastic deformation and failure mechanisms. The mechanical characterization results were compared to those obtained by the authors in previous works on conventional casting alloys Al–Si–Mg and Al–Si–Mg–Cu.

The following conclusions can be drawn. 1) The T5 alloy shows an appreciable residual hardness with a minimum value of 80 HB₁₀ after thermal exposure at 245 °C for 48 h. Under the same conditions, the T6R alloy shows a marked hardness decrease, up to a minimum value of 50 HB₁₀. 2) The T5 and T6R alloys, after overaging and high-temperature testing, show reduced mechanical strength. However, the decrease is less evident in the T5_{OA}-200T (–42% in YS value and –60% in UTS value) than in the T6R_{OA}-200T (–65% in YS value and 70% in UTS). On the contrary, ductility increases marginally for the T6R_{OA}-200T (+2% in ϵ_f) and significantly for the T5_{OA}-200T (+65% in ϵ_f). 3) The T5–RT shows a complete plastic

behavior, while the T6R-RT, T5_{OA}-200T, and T6R_{OA}-200T are characterized previously by a significant necking. At high temperatures, the strain-hardening coefficients decrease by 77% and 80% for the T5_{OA}-200T and T6R_{OA}-200T conditions, respectively, due to the thermal softening phenomena and the degradation of the strengthening mechanisms. 4) The sub-micrometric cellular structure of the T5 alloy imparts higher high-temperature mechanical properties compared to the composite-like microstructure of the T6R alloy due to the higher efficiency in hindering the dislocation motion. 5) The T5 alloy achieves mechanical properties superior to conventional Al-Si-Mg-casting alloys and slightly inferior to Al-Si-Cu-Mg alloys in both tested conditions (T5-RT and T5_{OA}-200T). Higher mechanical properties characterize the T6R-RT condition compared to the Al-Si-Mg alloys. However, the T6R_{OA}-200T condition shows a remarkable drop in strength properties (YS and UTS).

In conclusion, the T5 heat-treated L-PBF AlSi10Mg alloy can be considered a material to be used for applications up to 200 °C. However, further investigations, such as fatigue tests, must be carried out to fully evaluate the mechanical behavior and the potential of the L-PBF AlSi10Mg alloy at high temperatures.

Acknowledgements

This work was supported by the RIMMEL project, CUP B91F18000370009, POR FESR EMILIA ROMAGNA 2014-2020, Asse 1 - Ricerca e Innovazione. Open Access Funding provided by Universita degli Studi di Bologna within the CRUI-CARE Agreement.

Conflict of Interest

The authors declare no conflict of interest.

Data Availability Statement

The data that support the findings of this study are available from the corresponding author upon reasonable request.

Keywords

Al alloy, AlSi10Mg, high-temperature mechanical properties, laser-based powder bed fusion (L-PBF), microstructural characterization, overaging

Received: August 29, 2022

Revised: January 19, 2023

Published online:

- [1] B. DeBoer, N. Nguyen, F. Diba, A. Hosseini, *Int. J. Adv. Manuf. Technol.* **2021**, 115, 413.
- [2] R. Godina, I. Ribeiro, F. Matos, T. Ferreira, B. H. Carvalho, P. Peças, *Sustainability* **2020**, 12, 7066.
- [3] M. Rogante, V. T. Lebedev, F. Nicolaie, E. Retfalvi, L. Rosta, *Phys. B Condens. Matter*, **2005**, 358, 224.
- [4] E. Balducci, L. Ceschini, A. Morri, A. Morri, *J. Mater. Eng. Perform.* **2017**, 26, 3802.
- [5] M. Wong, S. Tsopanos, C. Sutcliffe, I. Owen, *Rapid Prototyping J.* **2017**, 13, 291.

- [6] E. O. Olakanmi, R. F. Cochrane, K. W. Dalgarno, *Progr. Mater. Sci.* **2015**, 74, 401.
- [7] T. DebRoy, H. L. Wei, J. S. Zuback, T. Mukherjee, J. W. Elmer, J. O. Milewski, A. M. Beese, A. Wilson-Heid, A. De, W. Zhang, *Progr. Mater. Sci.* **2018**, 92, 112.
- [8] M. Javidani, D. Larouche, *Int. Mater. Rev.* **2014**, 59, 132.
- [9] E. Balducci, L. Ceschini, S. Messieri, *JOM* **2018**, 70, 2716.
- [10] S. Katsikis, B. Noble, S. J. Harris, *Mater. Sci. Eng. A* **2008**, 485, 613.
- [11] D. Herzog, V. Seyda, E. Wycisk, C. Emmelmann, *Acta Mater.* **2016**, 117, 371.
- [12] E. Balducci, L. Ceschini, S. Messieri, S. Wenner, R. Holmestad, *Mater. Des.* **2017**, 119, 54.
- [13] A. P. Babu, A. Huang, N. Biribilis, *Mater. Sci. Eng. A* **2021**, 807, 140857.
- [14] M. S. Kenevisi, Y. Yu, F. Lin, *Mater. Sci. Technol.* **2021**, 37, 805.
- [15] S. Toschi, E. Balducci, L. Ceschini, E. A. Mørtsell, A. Morri, M. Di Sabatino, *Metals* **2019**, 9, 130.
- [16] A. Iturrioz, E. Gil, M. M. Petite, F. Garciandia, A. M. Mancisidor, M. San Sebastian, *Weld World* **2018**, 62, 885.
- [17] L. Zhou, A. Mehta, E. Schulz, B. McWilliams, K. Cho, Y. Sohn, *Mater. Charact.* **2018**, 143, 5.
- [18] E. Cerri, E. Ghio, G. Bolelli, *J. Mater. Eng. Perform.* **2021**, 30, 4981.
- [19] I. Rosenthal, R. Shneck, A. Stern, *Mater. Sci. Eng. A* **2018**, 729, 310.
- [20] E. Padovano, C. Badini, A. Pantarelli, F. Gili, F. D'Aiuto, *J. Alloys Compd.* **2020**, 831, 154822.
- [21] W. Li, S. Li, J. Liu, A. Zhang, Y. Zhou, Q. Wei, C. Yan, Y. Shi, *Mater. Sci. Eng. A* **2016**, 663, 116.
- [22] G. Di Egidio, L. Ceschini, A. Morri, C. Martini, M. Merlin, *Metall. Mater. Trans. B* **2022**, 53, 284.
- [23] N. E. Uzan, R. Shneck, O. Yehekel, N. Frage, *Addit. Manuf.* **2018**, 24, 257.
- [24] D. Lehmhus, T. Rahn, A. Struss, P. Gromzig, T. Wischeropp, H. Becker, *Materials* **2022**, 15, 7386.
- [25] M. Tocci, A. Varone, R. Montanari, A. Pola, *Mater. Sci. Forum* **2021**, 1016, 1485.
- [26] Y. Cao, X. Lin, Q. Z. Wang, S. Q. Shi, L. Ma, N. Kang, W. D. Huang, *J. Mater. Sci. Technol.* **2021**, 62, 162.
- [27] L. Ceschini, A. Morri, S. Toschi, S. Seifeddine, *Mater. Sci. Eng. A* **2016**, 653, 129.
- [28] A. Morri, L. Ceschini, S. Messieri, E. Cerri, S. Toschi, *Metals* **2018**, 8, 393.
- [29] L. Ceschini, A. Morri, S. Toschi, S. Johansson, S. Seifeddine, *Mater. Sci. Eng. A* **2015**, 648, 340.
- [30] L. Ceschini, S. Messieri, A. Morri, S. Seifeddine, S. Toschi, M. Zamani, *Trans. Nonferrous Met. Soc.* **2020**, 30, 2861.
- [31] ASTM E10-18, Standard Test Method for Brinell Hardness of Metallic Materials, ASTM International, West Conshohocken, PA, **2018**.
- [32] ASTM E3-11, Standard Guide for Preparation of Metallographic Specimens, ASM International, West Conshohocken, PA, **2017**.
- [33]] ASTM 407-07, Standard Practice for Microetching Metals and Alloys, ASM International, West Conshohocken, PA, **2015**.
- [34] M. Li, S. Ghosh, O. Richmond, H. Weiland, T. N. Rouns, *Mater. Sci. Eng. A* **1999**, 265, 153.
- [35] ISO 6892-1, Metallic Materials - Tensile Testing - Part 1: Method of Test at Room Temperature, International Organization for Standardization, Geneva, Switzerland, **2019**.
- [36] ISO 6892-2, Metallic materials - Tensile testing - Part 2: Method of test at elevated temperature, International Organization for Standardization, Geneva, Switzerland, **2018**.
- [37] P. Dai, X. Luo, Y. Yang, Z. Kou, B. Huang, J. Zang, J. Ru, *Prog. Nat. Sci.* **2020**, 30 63.
- [38] ISO 10275, Metallic materials - Sheet and strip - Determination of Tensile Strain Hardening Exponent, International Organization for Standardization, Geneva, Switzerland, **2020**.
- [39] M. Fousová, D. Dvorský, A. Michalcová, D. Vojtěch, *Mater. Charact.* **2018**, 137, 119.

- [40] J. Fiocchi, A. Tuissi, P. Bassani, C. A. Biffi, *J. Alloys Compd.* **2017**, *695*, 3402.
- [41] J. Fite, S. E. Prameela, J. A. Slotwinski, T. P. Weihs, *Addit. Manuf.* **2020**, *36*, 101429.
- [42] B. Chen, S. K. Moon, X. Yao, G. Bi, J. Shen, J. Umeda, K. Kondoh, *Scr. Mater.* **2017**, *141*, 45.
- [43] A. Hadadzadeh, B. S. Amirkhiz, M. Mohammadi, *Mater. Sci. Eng. A* **2019**, *739*, 295.
- [44] F. Alghamdi, X. Song, A. Hadadzadeh, B. Shalchi-Amirkhiz, M. Mohammadi, M. Haghshenas, *Mater. Sci. Eng. A* **2020**, *783*, 139296.
- [45] M. Tocci, A. Pola, M. Gelfi, G. M. La Vecchia, *Metall. Mater. Trans. B* **2020**, *51*, 4799.
- [46] L. F. Wang, J. Sun, X. L. Yu, Y. Shi, X. G. Zhu, L. Y. Cheng, H. H. Liang, B. Yan, L. J. Guo, *Mater. Sci. Eng. A* **2018**, *734*, 299.
- [47] L. Tonelli, E. Liverani, A. Morri, L. Ceschini, *Metall. Mater. Trans. B* **2021**, *52*, 484.
- [48] N. T. Aboulkhair, I. Maskery, C. Tuck, I. Ashcroft, N. M. Everitt, *Mater. Sci. Eng. A* **2016**, *667*, 139.
- [49] L. Ceschini, A. Morri, A. Morri, S. Toschi, S. Johansson, S. Seifeddine, *Mater. Des.* **2015**, *83*, 626.
- [50] M. Tocci, R. Donnini, G. Angella, E. Gariboldi, A. Pola, *J. Mater. Eng. Perform.* **2019**, *28*, 7097.
- [51] E. Gariboldi, J. N. Lemke, L. Rovatti, O. Baer, G. Timelli, F. Bonollo, *Metals* **2018**, *8*, 348.
- [52] J. Delahaye, J. Tchoufang Tchoundjang, J. Lecomte-Beckers, O. Rigo, A. M. Habraken, A. Mertens, *Acta Mater.* **2019**, *175*, 160.
- [53] P. J. Moses, Q. Liu, J. P. Best, X. Li, J. J. Kruzic, U. Ramamurty, B. Gludovatz, *Acta Mater.* **2021**, *211*, 116869.
- [54] *Handbook of Aluminum* (Eds: G.E. Totten, D.S. MacKenzie), 1st ed., Vol. 2, Alloy Production and Materials Manufacturing, CRC Press, Boca Raton FL **2003**.
- [55] M. Colombo, E. Gariboldi, A. Morri, *Mater. Sci. Eng. A* **2018**, *713*, 151.
- [56] D. Broek, *Eng. Fract. Mech.* **1973**, *5*, 55.
- [57] W. H. Kan, Y. Nadot, M. Foley, L. Ridosz, G. Proust, J. M. Cairney, *Addit. Manuf.* **2019**, *29*, 100805.
- [58] S. Joseph, S. Kumar, *Mater. Sci. Eng. A* **2013**, *588*, 111.
- [59] M. T. Di Giovanni, J. T. Oliveira de Menezes, G. Bolelli, E. Cerri, E. M. Castrodeza, *Eng. Fract. Mech.* **2019**, *217*, 106564.
- [60] A. R. Farkoosh, M. Pegguleryuz, *Mater. Sci. Eng. A* **2015**, *621*, 277.
- [61] A. Aversa, G. Marchese, A. Saboori, E. Bassini, D. Manfredi, S. Biamino, D. Ugues, P. Fino, M. Lombardi, *Materials* **2019**, *12*, 1007.